Journal of Materials Chemistry B

PAPER

View Article Online
View Journal | View Issue

Cite this: J. Mater. Chem. B, 2014, 2, 5378

Robocasting of biomimetic hydroxyapatite scaffolds using self-setting inks†

Y. Maazouz,[ab] E. B. Montufar,[ab] J. Guillem-Marti,[ab] I. Fleps,[a] C. Öhman,[c] C. Persson[c] and M. P. Ginebra*[ab]

Received 18th March 2014
Accepted 9th June 2014

DOI: 10.1039/c4tb00438h

www.rsc.org/MaterialsB

Low temperature self-setting ceramic inks have been scarcely investigated for solid freeform fabrication processes. This work deals with the robocasting of alpha-tricalcium phosphate/gelatine reactive slurries as a bioinspired self-setting ink for the production of biomimetic hydroxyapatite/gelatine scaffolds. A controlled and totally interconnected pore network of ~300 μm was obtained after ink printing and setting, with the struts consisting of a micro/nanoporous matrix of needle-shaped calcium deficient hydroxyapatite crystals, with a high specific surface area. Gelatine was effectively retained by chemical crosslinking. The setting reaction of the ink resulted in a significant increase of both the elastic modulus and the compressive strength of the scaffolds, which were within the range of the human trabecular bone. In addition to delaying the onset of the setting reaction, thus providing enough time for printing, gelatine provided the viscoelastic properties to the strands to support their own weight, and additionally enhanced mesenchymal stem cell adhesion and proliferation on the surface of the scaffold. Altogether this new processing approach opens good perspectives for the design of hydroxyapatite scaffolds for bone tissue engineering with enhanced reactivity and resorption rate.

1. Introduction

The architecture of scaffolds for tissue engineering is of critical importance to allow for cellular penetration, adequate diffusion of nutrients and waste products, and angiogenesis.[1] Solid free-form fabrication techniques have gained an increasing interest in the biomaterials community since they allow the fabrication of complex three-dimensional (3D) structures with a precise control of their dimensions from the micro to the millimetre scale.[2] Among them, robocasting or direct ink deposition allows 3D structures to be built layer-by-layer following a computer-aided design (CAD) model, through the deposition of concentrated ceramic slurries or polymeric inks that, in addition to being fully injectable, must be capable of supporting their own weight during assembly.[2,3] In the specific case of ceramic scaffolds, a sintering step is applied after printing the green body. High temperature sintered calcium phosphates, such as hydroxyapatite (HA), beta tricalcium phosphate (β-TCP) or even bioglass, have been employed to develop robocasted scaffolds for bone tissue engineering.[4–7] However, the low biodegradability of some of these high-temperature ceramics, particularly HA, represents a serious drawback when considering its application in bone tissue engineering, where the scaffold must be degraded and progressively replaced by a new bone.

In this work we aim at developing a self-setting ceramic ink that avoids the sintering step in the robocasted ceramic scaffolds. This strategy may allow the fabrication of biomimetic scaffolds, with a composition, crystallinity and microstructure that are much closer to the mineral phase of bone than the high-temperature robocasted ceramics, and particularly with a higher resorption rate than sintered hydroxyapatite scaffolds.[8] The basis for this development can be found in the chemistry of calcium phosphate cements. The setting mechanism of these materials is a dissolution–precipitation reaction that somehow mimics the phenomena taking place during the biomineralization process *in vivo*.[8] Furthermore, the low-temperature setting offers an outstanding platform for the incorporation of biologically active molecules that can be used to foster osteoinduction.[9]

While it is clear that the combination of the high structure accuracy and reproducibility provided by robocasting,[10] with the microstructural and compositional features of low-temperature setting ceramics can be a great benefit, the development of self-setting inks is a challenge, and has been scarcely investigated. One strategy proposed by Lode *et al.* consisted in using a non-reactive paste based on a non-aqueous liquid containing short

[a]Biomaterials, Biomechanics and Tissue Engineering Group, Department of Materials Science and Metallurgical Engineering, Technical University of Catalonia, Av. Diagonal 647, 08028, Spain. E-mail: maria.pau.ginebra@upc.edu; Fax: +34 934016706; Tel: +34 934017706

[b]Biomedical Research Networking Center in Bioengineering, Biomaterials and Nanomedicine (CIBER-BBN), Maria de Luna 11, Ed. CEEI, 50118 Zaragoza, Spain

[c]Division of Applied Materials Science, Department of Engineering Sciences, Uppsala University, Sweden

† Electronic supplementary information (ESI) available. See DOI: 10.1039/c4tb00438h

lipids and a surfactant, combined with ceramic particles.[11,12] The consolidation of the scaffold was triggered by hydrolysis of the ceramic component after the exchange of the non-aqueous liquid by water upon immersion in an aqueous solution.

In this work we intend to develop water-based ceramic inks containing reactive ceramic particles, capable of promoting a self-setting reaction, with the appropriate viscoelastic properties to be used for robocasting. The ability to extrude the ink is one of the critical aspects, especially when the reactivity of the particles can modify the rheological behaviour over time, and reduce considerably their printability.[13] Moreover, in addition to the basic requirements of ceramic inks for robocasting, such as low extrusion force without phase separation and shape retention after extrusion, the additives used in self-setting inks should neither hamper cement reactivity nor compromise the material biocompatibility.

Based on our previous knowledge on calcium phosphate cements, we selected alpha-tricalcium phosphate (α-TCP, α-$Ca_3(PO_4)_2$) as the reactive phase for the ink. α-TCP is one of the most commonly used components of calcium phosphate cements. When mixed with water it spontaneously hydrolyses to a calcium deficient hydroxyapatite (CDHA) according to the following reaction:[14]

$$3\alpha\text{-}Ca_3(PO_4)_2 + H_2O \rightarrow Ca_9(HPO_4)(PO_4)_5OH \quad (1)$$

One of the strategies to increase the injectability of calcium phosphate cements is the addition of a water-soluble polymer in the liquid phase. In a previous work we showed that the addition of gelatine improves significantly the injectability of calcium phosphate cement, and introduces an induction time for the onset of the setting reaction.[15] In addition, the combination of gelatine with calcium phosphate cements has been shown to yield significant benefits both in the processability and enhancement of the mechanical properties[15–19] and in the biological response.[20–23] Our hypothesis was that the gelling capacity of gelatine could also provide the viscoelasticity and the support needed for the build-up of the 3D-structure, while mimicking also the composite nature of bone, as it comes from the denaturation of collagen.[24] Therefore, in this study, a reactive ink based on gelatine combined with α-TCP is presented and its application for robocasting technology is demonstrated.

2. Experimental

2.1. Self-setting ink preparation

A mixture of calcium carbonate ($CaCO_3$, Sigma-Aldrich C4830) and monetite ($CaHPO_4$, Sigma-Aldrich C7263), with a Ca/P molar ratio of 1.5 was used to synthesize α-TCP in a furnace (Hobersal CNR-58, Barcelona, Spain) at 1400 °C, followed by quenching in air. In addition, also the polymorph stable at room temperature, *i.e.* beta tricalcium phosphate (β-TCP, β-$Ca_3(PO_4)_2$) was synthesized from the same reactants at 1100 °C, and was left to cool down in the furnace. The two polymorphs, that have different solubilities ($-\log K_s = 28.9$ and 25.5 at 25 °C for β-TCP and α-TCP respectively) were used to identify the role of the setting reaction and gelatine gelation on the extrudability of the inks. Powders were prepared by milling the materials in a planetary mill (Fritsch Pulverisette, Germany) using agate bowl and balls, following a three-step protocol: first milling for 60 min at 450 rpm with 10 balls ($d = 30$ mm); second, milling for 40 min at 500 rpm with 10 balls ($d = 30$ mm); and third, milling for 60 min at 500 rpm with 100 balls ($d = 10$ mm). A 10 wt% gelatine aqueous solution was prepared by mixing deionized water and type B bovine gelatine (250-LB, Rousselot) at 60 °C until total dissolution. The gelatine solution was then used as the liquid phase to prepare either reactive or non-reactive inks, using α-TCP or β-TCP as the ceramic component respectively. Powder and liquid were mixed in a dual centrifugal asymmetric mixer (DCAM; SpeedMixer DAC-150 FZK) during 1.5 min at 3000 rpm at a liquid to powder ratio (L/P) of 0.65 ml g^{-1}. The prepared ink was introduced into 3 ml syringes (Nordson Optimum®) and centrifuged for 30 s at 3000 rpm in the DCAM in order to remove air bubbles.

2.2. Extrusion tests

α-TCP/gelatine and β-TCP/gelatine ink-filled syringes coupled to a tapered tip with an inner diameter of 840 μm (Nordson, EFD) were placed into a customized extrusion test set-up for a universal testing machine (BIONIX, MTS). α-TCP/water suspensions with the same L/P (0.65 ml g^{-1}) were used as the control material. The extrusion load was recorded as a function of the plunger displacement, at a constant plunger rate of 0.15 mm s^{-1}. The extrusion was started at different time points after mixing the solid and the liquid phases (between 5 and 400 min), and the test was stopped when the applied load reached 500 N. The extrusion force was determined by averaging the plateau zone of the extrusion curve as described elsewhere,[13] and plotted as a function of time after mixing both TCP polymorph inks. The evolution of temperature of the inks after mixing was recorded by introducing a thermocouple within the syringe.

2.3. Robocasting of self-setting inks

3D scaffolds (parallelepipeds of 5 × 5 × 5 mm^3 or 5 × 5 × 10 mm^3) with orthogonal layers were robocasted using a rapid prototyping machine (3Dn Series, nScrypt, USA) and tapered tips with an inner diameter of 840 μm (Nordson EFD). The α-TCP/gelatine ink was dispensed onto poly(tetrafluoroethylene) sheets using the displacement pump device, controlling the plunger rate at 0.09 mm s^{-1} and the individual axial movement rate at 15 mm s^{-1}. An orthogonal pattern with a horizontal strand to strand centre spacing of 1140 μm (X and Y direction) and a vertical (Z direction) spacing of 500 μm was used, which corresponds to a horizontal spacing of 300 μm. Scaffolds were printed after 15 min of post-mixing time. Robocasted scaffolds were left to dry overnight at room temperature and 50% of relative humidity. The samples after drying are referred to as "as-printed" from now on.

2.4. Setting and crosslinking

Part of the as-printed samples was immersed in a mixture of EDC ((1-ethyl-3-(3-dimethylaminopropyl))carbodiimide, Sigma

Aldrich) and NHS (*N*-hydroxysuccinimide, Sigma Aldrich) at a 2 : 1 molar ratio in water overnight at 4 °C, as described in ref. 16, in order to covalently crosslink the gelatine. Both crosslinked and non-crosslinked scaffolds were allowed to set by immersing them in distilled water at room temperature for 7 days.

2.5. Robocasted scaffold characterization

Microcomputed tomography (μ-CT, SkyScan 1172, Bruker, Kontich, Belgium) imaging was performed on 6 crosslinked and 6 non-crosslinked set scaffolds in order to assess the macroporosity architecture, using the following conditions: source voltage 100 kV; current 100 μA; aluminium and copper filter; frame averaging 4; and isotropic pixel size 15 μm^2. Reconstruction of cross-sections was done using software package NRecon (SkyScan, Bruker, Kontich, Belgium). The reconstructed images were binarized to separate the scaffold from the surrounding air using an optimized global threshold and structural analysis was done in software package CTAn (SkyScan, Bruker, Kontich, Belgium). 3D reconstructions of the samples were obtained using CTvox (SkyScan, Bruker, Kontich, Belgium). A volume of interest of $5 \times 5 \times 5$ mm^3 was extracted and the porosity was selected to be represented from two perspectives, upper view (*Z* direction) and lateral view (*Y* direction). In addition, *in situ* monitored uniaxial compressive tests were performed on parallelepiped samples ($5 \times 5 \times 10$ mm^3) along the *Z* direction in order to observe the failure mechanism of the robocasted scaffolds. A displacement of 0.2 mm was imposed step by step until total failure of the sample. Solid rendered broken scaffolds are presented from vertical and lateral perspectives.

Open porosity and pore size distribution were also analysed by mercury intrusion porosimetry (MIP, AutoPore IV Micromeritics), in the range between 0.006 and 360 μm.

The microstructure of the scaffolds was observed under a field emission scanning electron microscope (FIB/SEM, Zeiss Neon 40) at 5 kV, after coating the surface with a thin gold/palladium layer.

Phase composition was assessed by X-ray powder diffraction (D8 Advance, Bruker) on the powder obtained for each condition of setting and crosslinking after crushing the scaffolds in an agate mortar. The diffractometer equipped with a Cu K_α X-ray tube was operated at 40 kV and 40 mA. Data were collected in 0.02° steps over the 2θ range of 10–80° with a counting time of 2 s per step. Phase quantification was performed using the reference intensity ratio method (EVA, Bruker) comparing diffraction patterns of the crystalline structures of calcium deficient hydroxyapatite (CDHA; ICDD 01-086-1201) and α-TCP (ICDD 00-029-0359). Fourier transform infrared spectroscopic studies (FTIR Nicolet 6700, Thermo Scientific) were also carried out on samples embedded in KBr pellets in order to assess the presence of the different functional groups. The specific surface area (SSA) of the set scaffolds was determined by nitrogen adsorption according to the Brunauer–Emmet–Teller (BET) method (ASAP 2020, Micromeritics). The skeletal density of the set scaffolds was determined using helium pycnometry (AccuPyc 1340, Micromeritics, UK) using 10 purges and 10 runs.

The compressive strength of the robocasted scaffolds was determined on $5 \times 5 \times 5$ mm^3 cubes ($n = 8$ for each condition) perpendicular to the printing plane (in the *Z* direction) by applying a uniaxial compressive load, using a universal testing machine (Bionix, MTS) at a displacement rate of 1 mm min^{-1}.

2.6. Gelatine release during alpha tricalcium phosphate setting

Dense cylinders (6 mm diameter × 6 mm high) were prepared with either the α-TCP/gelatine ink or with α-TCP mixed with deionized water, by filling Teflon moulds with the help of a spatula. Half of the α-TCP/gelatine cylinders were crosslinked according to Section 2.4. While the setting reaction was taking place, the cylinders were immersed immediately after preparation in phosphate-buffered saline (PBS, Invitrogen; 2 ml of PBS per sample), in customized 48-well plates, in order to monitor the release of gelatine. Previously, a channel between wells was thermoformed in order to allow the transfer of medium between two adjacent wells, one containing the material and the other left blank. The cumulative release of gelatine until 7 days was monitored continuously by spectrophotometry, recording the optical absorbance of the immersion media in the blank well at 230 nm (M200 PRO Microplate reader, Tecan). Crosslinked and non-crosslinked α-TCP/gelatine specimens, as well as α-TCP/water samples were tested in six replicates each. A calibration curve with decreasing concentrations of gelatine was obtained. The quantity of gelatine released was normalized with respect to the total amount of gelatine in the samples.

2.7. Cell proliferation test

Rat mesenchymal stem cells (rMSCs) were isolated from the femurs and tibias of Lewis rats and expanded *in vitro*. Discs of 15 mm diameter × 2 mm high were prepared by moulding α-TCP/gelatine inks, as well as α-TCP/water pastes in Teflon moulds as described in Section 2.6. Half of the α-TCP/gelatine discs were subjected to the crosslinking protocol described in Section 2.4. After setting for 7 days in distilled water, 6 discs of each condition were placed in 24-well plates and immersed for 30 min in 70% ethanol for sterilization, followed by three rinsing steps with PBS and incubation over-night with the complete cell culture medium (Advanced Dulbecco's modified Eagle's medium, advDMEM; Invitrogen), supplemented with 15% fetal bovine serum (FBS), penicillin/streptomycin (50 U ml^{-1} and 50 μg ml^{-1}, respectively), L-glutamine (2 mM) and HEPES buffer (20 mM). The following day the cell culture medium was discarded and subconfluent rMSCs in passage 6 were trypsinized, centrifuged and seeded at a density of 50 000 cells per well. Tissue culture polystyrene (TCPS) was used as the control surface for cell culture. After 5 h, 24 h and 7 days of culture the samples were transferred to new 24-well plates and washed with PBS to remove unattached cells, and attached cells were lysed with 500 μl of M-PER® (Mammalian Protein Extraction Reagent; Thermo Scientific). The cell number was evaluated by using a LDH Cytotoxicity Detection Kit (Roche Applied Science) following the manufacturer's instructions. The LDH activity was measured spectrophotometrically with a plate

reader at 492 nm (M200 PRO Microplate reader, Tecan). To express the results in cell number a calibration curve with decreasing number of cells was obtained.

The cell morphology was observed by SEM (Zeiss Neon 40) after 5 h of culture. The discs containing the cells were washed with PBS (×3) and fixed for 1 h at 4 °C in a 2.5% glutaraldehyde solution in PBS. Subsequently, fixed samples were washed with PBS (×3), and dehydrated in 50, 70, 90, 96 and 100% ethanol series. Complete dehydration was performed in hexamethyldisilazane (HMDS) and discs were stored inside a desiccator. Prior to SEM observations the dried discs were covered with a thin gold–palladium layer to prevent electrical charge.

2.8. Statistical analysis

A *t*-student test assuming equal variances ($\alpha = 0.05$) was performed to analyse the statistical significance of the results of macroporosity and mechanical properties of the set scaffolds. Multifactorial ANOVA was used to determine the statistical significance of the results obtained in the cell culture study, with a significance level of $p = 0.05$.

3. Results and discussion

3.1. Gelatine based inks and extrusion tests

Extrusion tests were performed with the gelatine inks loaded either with α-TCP or β-TCP powders. This was done to identify the role of the gelling of gelatine and the self-setting reaction of the ceramic phase. α-TCP can be considered as a "reactive" powder, because it is known to spontaneously hydrolyse to a calcium deficient hydroxyapatite in contact with water at room temperature. In contrast, β-TCP can be considered as "non-reactive" under these conditions, since due to its lower solubility it does not hydrolyse and therefore it does not give rise to a self-setting reaction.[13]

Extrusion forces of both α-TCP and β-TCP/gelatine-inks increased sharply during the first 100 min after mixing (Fig. 1), whereas in the α-TCP suspension prepared with water they remained very low until 550 min after mixing. Thus, the initial increase in extrusion force in the α-TCP and β-TCP/gelatine-inks can be attributed to the gelling of the gelatine upon cooling of the ink inside the syringe, which induced a transition from a random coil conformation (sol state) to the formation of triple helices (gel state).[25,26] The cooling curves of the two TCP/gelatine inks are shown in the ESI (Fig. S1).† Just after mixing the temperature of the gelatine-based-inks was around 28 °C, and then the temperature decreased over time until room temperature (around 22.5 °C in our laboratory), in approximately 30 minutes. After 200 min, a gradual increase of the extrusion force was observed in the case of the α-TCP/gelatine ink, whereas a stabilization of the extrusion force was recorded in the case of β-TCP/gelatine ink. This second increase of the extrusion force can be associated with the setting reaction of the α-TCP, caused by formation of an entangled network of CDHA crystals, which has been described as a factor hindering the extrusion of α-TCP pastes.[13] This phenomenon was observed also in the α-TCP/water suspension, but only after a long induction time. The long

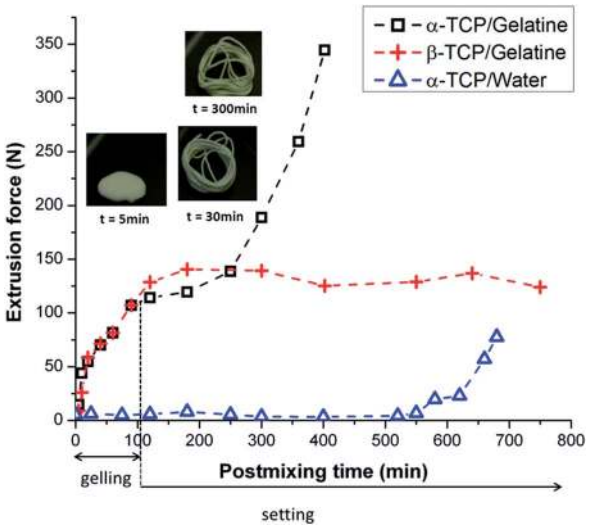

Fig. 1 Mean extrusion force of reactive (α-TCP) and non-reactive (β-TCP) inks as a function of post-mixing time. Inks were prepared either with or without gelatine. The inset pictures show the aspects of the extruded material at three different post-mixing times. The standard deviations for each time point were too small to be properly represented.

induction period compared to what was found in a previous study with similar pastes[13] can be explained by the much higher L/P ratio used in the present work. The fact that the increase in extrusion force associated with the hydrolysis of α-TCP was observed earlier for the gelatine-based ink suggests an accelerating effect in the setting reaction, as proposed by Bigi *et al.*,[17,18] who claimed a nucleation effect of gelatine on the precipitation of CDHA. Shape retention of the extruded inks was very low after short post-mixing times (see insets in Fig. 1). The extruded strands were able to maintain their shape only after 15 min, because of the increment of viscosity due to the gelling of gelatine. An important issue was to determine the time frame during which the paste could be used for robocasting. In the case of the α-TCP self-setting ink the window of processing was smaller than for the non-reactive β-TCP ink. Although the α-TCP ink can be completely extruded until 400 min, it is strongly recommended to print it between 15 and 30 min post-mixing, when the forces are still low. Above 30 min the paste can be extruded but there is limited adhesion between strands. Extruding the α-TCP ink after 200 min could result in disrupting the interlocking of the growing CDHA crystals, compromising the mechanical strength of the scaffold. In contrast, the β-TCP ink can be printed for a longer period of time, offering the possibility of storing the ink and printing it off the shelf. For the two TCP polymorphs, the inks were totally injectable over the printing process (around 3 min for the samples tested in this study).

3.2. Scaffold architecture and porosity

Set robocasted α-TCP/gelatine scaffolds presented a well-defined and totally interconnected orthogonal network of macropores (Fig. 2). The macroporous structure was not

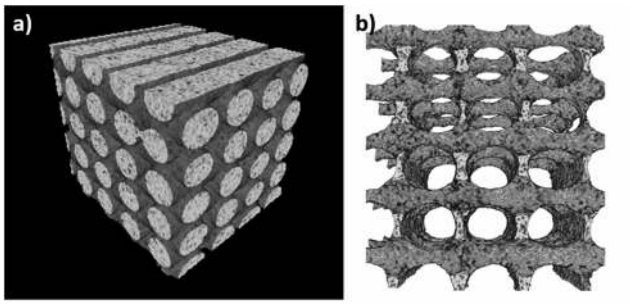

e)

Object	Size (µm)
Strand	850 ± 50
Pore X or Y direction	310 ± 20
Pore Z direction	170 ± 40

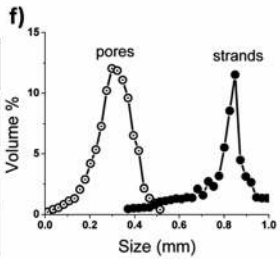

Fig. 2 (a) Robocasted scaffold architecture reconstructed from µ-CT scans. (b) Solid rendered pore architecture represented from a lateral view, showing a totally interconnected orthogonal network of macropores of controlled size and shape. No significant differences were found in total macroporosity and macropore dimensions between the two different crosslinking conditions; (c) and (d) SEM micrographs of the as-printed scaffolds from two different perspectives; (e) mean macropore and strand sizes and standard deviations determined by image analysis of SEM micrographs; (f) macropore size distribution (open circles) and strand diameter distribution (full circles) of the robocasted scaffolds as determined by µ-CT.

modified upon crosslinking. Total macroporosites of 18.7 ± 0.3% for non-crosslinked and 18.0 ± 0.2% for crosslinked samples were determined from the µ-CT scans, with no statistically significant differences among them ($p > 0.05$). Fig. 2e reports the strand and pore dimensions according to SEM images, whereas the macropore size distribution and strand diameter distribution determined by µ-CT are shown in Fig. 2f. The mode of the strand diameter distribution was at 850 µm, matching with the size of the printing tip used. The size distribution of the macropores was wider, since in fact the dimensions were different in different directions: 310 ± 20 µm in the *X* and *Y* directions, and 170 ± 40 µm in the *Z* direction, in good agreement with the printing pattern.

In addition to the macroporosity being incorporated and controlled by the robocasting fabrication process, the scaffold strands were expected to present an important volume of micro/nanoporosity coming from the spaces between CDHA crystals precipitated during the setting reaction. Since this micro/nanoporosity is beyond the spatial resolution of µ-CT, it was analysed by MIP (Fig. 3), and compared with a reference material without gelatine (α-TCP/water). All materials showed open porosity at the submicron or nanoscale range, which correspond to the spaces between the CDHA crystal network formed during the setting reaction.[27] The total micro/nanoporosity was smaller in the set scaffolds containing gelatine when compared with the fully inorganic material, and also the pore entrance size distribution was smaller, more markedly when gelatine had been crosslinked. Thus, the pore entrance size distribution of the crosslinked sample was narrow, with pore entrance sizes smaller than 100 nm. This can be related to the presence of gelatine between the CDHA crystals, to a higher extent in the crosslinked samples. Combining the results of µ-CT (pores bigger than 15 µm) and MIP (pores smaller than 15 µm), the total porosities of the crosslinked and non-crosslinked scaffolds were approximately 60 and 65% (respectively), the difference arising from the different percentages of micro/nanoporosity.

3.3. Scaffold microstructure, phase composition and gelatine crosslinking

The XRD patterns displayed in Fig. 4a showed that the as-printed scaffolds were mainly composed of α-TCP, with only a small amount of CDHA (8.1 ± 0.1%). This indicates that during the process of printing and drying most α-TCP remained unreacted. The set scaffolds, both the crosslinked and non-crosslinked ones, consisted of phase-pure CDHA, meaning that

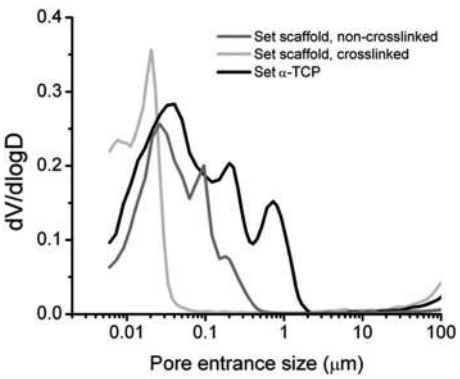

	Micro/ nanoporosity (%)	Pore entrance size range (µm)
Set Scaffold, Non-crosslinked	45.8	<0.5µm
Set Scaffold, crosslinked	41.4	<0.1µm
Set α-TCP	55.7	<2.0µm

Fig. 3 Pore entrance size distribution determined by MIP for non-crosslinked set scaffolds (dark grey line), crosslinked set scaffolds (light grey line) and the reference material without gelatine (black line). The total micro/nanoporosity of the scaffolds and the reference material, together with their corresponding pore entrance size range is displayed in the table below.

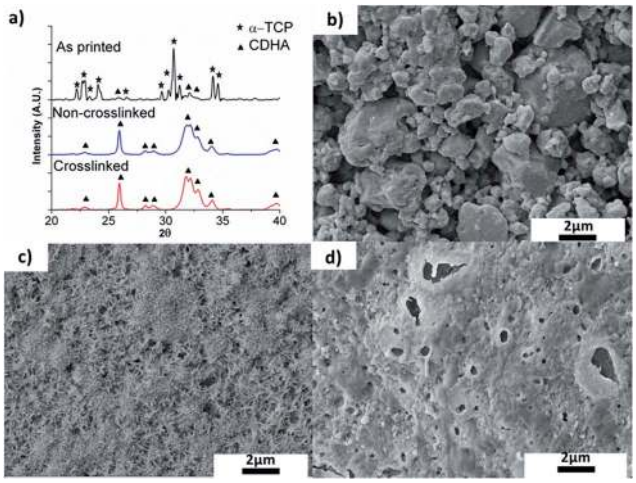

Fig. 4 (a) X-ray diffraction patterns of as-printed (black) and set robocasted scaffolds (7 days of setting), both non-crosslinked (blue) and crosslinked (red). The stars and squares represent the reference diffraction patterns of α-TCP and CDHA, respectively. Indexed diffractograms are provided in the ESI (Fig. S2).† SEM micrographs on the surface of the strands in the scaffolds are shown in (b) as-printed, (c) non-crosslinked, and (d) crosslinked set scaffolds.

α-TCP was totally hydrolysed, and that the gelatine crosslinking did not prevent the hydrolysis process. The indexed diffractograms are provided in the ESI (Fig. S2).† Further information about the kinetics of the hydrolysis of α-TCP into CDHA, and the crystallographic structure of the end product can be found in the literature.[14,28,29]

Regarding the FTIR results (Fig. 5), the patterns of the set scaffolds showed typical bands of the hydroxyapatite phase characterized by the OH stretching band (~3570 cm^{-1}) and the different vibration modes for PO_4 ($\nu_1 \sim 960$, $\nu_3 \sim 1040$ and

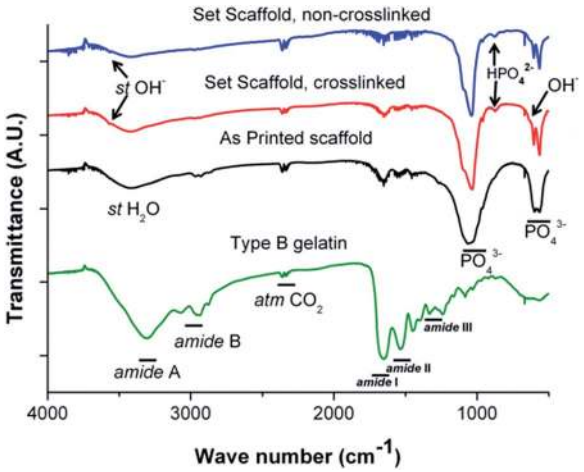

Fig. 5 FTIR spectra of pure gelatine (green), as-printed scaffold (black), set crosslinked scaffold (red) and set non-crosslinked scaffold (blue). The intensity of the characteristic amide stretch bands and vibrations of gelatine (A, B; I, II, III) decreased upon setting, more markedly in the non-crosslinked scaffold. Furthermore, the characteristic bands for OH^- and HPO_4^- of CDHA were detected in the set scaffolds.

$\nu_4 \sim 603$ and ~565 cm^{-1}). The small band appearing at ~870 cm^{-1} accounts for the presence of HPO_4, which is typical in CDHA.[14] The poorly resolved bands in the spectra are an indication of low range atomic local ordering revealing the defective nature (*e.g.* presence of vacancies and/or ion substitutions in the lattice) of the sample. The presence of the amide stretch bands (A, 3310–3270 cm^{-1}; B, 3100–3030 cm^{-1}) and vibrations (I, 1600–1700 cm^{-1}; II, 1450–1600 cm^{-1}; III, 1450–1300 cm^{-1})[30] characteristic of gelatine, in both the as-printed and crosslinked set scaffolds, demonstrated that the crosslinking reaction was able to retain the gelatine to a large extent, throughout the setting reaction. In contrast, these bands drastically decreased in intensity upon setting in the non-crosslinked scaffolds, suggesting that a significant proportion of the gelatine was dissolved during the setting process.

To confirm this hypothesis, the release of gelatine in the incubation medium during the setting process was measured by spectrophotometry. The release profile (Fig. 6) shows that although gelatine was released in both types of scaffolds, the total amount and the release kinetics was drastically reduced when gelatine was crosslinked. The experimental data were fit to the power law proposed by Korsmeyer–Peppas:[31]

$$\mathrm{CR} = (M(t))/M_\infty = kt^b \quad (2)$$

where: CR is the cumulative release; $M(t)$ is the quantity released at time t; M_∞ is the amount released for an infinite time of the experiment; k is a constant accounting for the properties of the matrix and the diffusing molecules; t is the time of release; and b is the diffusional exponent characteristic of the release mechanism.

For the non-crosslinked samples, an exponent b of 0.40 was found, close to that corresponding to pure Fickian diffusion, and 48.69% of the gelatine was released after 7 days. With gelatine crosslinking, the exponent b decreased to a value of 0.23, and the relative amount of gelatine released after 7 days was only 22.08%, confirming the higher retention of gelatine in the material.

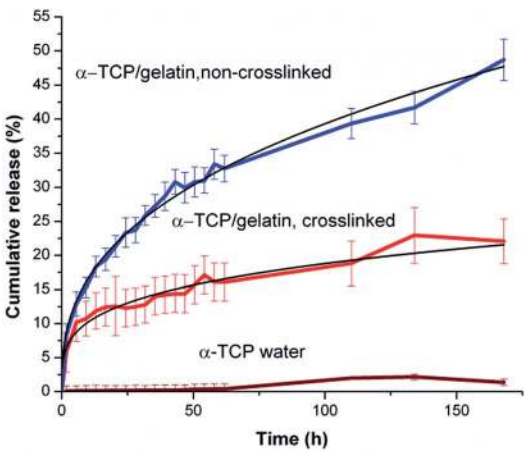

Fig. 6 Cumulative release of gelatine during setting for the non-crosslinked (blue) and crosslinked (red) samples, together with the reference material without gelatine (brown). The black line corresponds to the data fitting with the Korsmeyer–Peppas model (eqn (2)).

In congruence with the FTIR and gelatine release results, SEM micrographs of the non-crosslinked set scaffolds (Fig. 4c), showed no apparent traces of gelatine on the surface. The microstructure consisted of an entangled network of nanosized needle-shaped CDHA crystals, characteristic of a self-setting hydrolysis reaction of α-TCP.[27] In contrast, gelatine was clearly visible on the surface of the crosslinked set scaffolds, covering almost totally the inorganic crystals (Fig. 4d). The as-printed samples presented a microstructure composed of aggregates of α-TCP particles without clear evidence of a new precipitated phase (Fig. 4b), confirming a very limited reaction during the printing and drying steps.

The skeletal densities further corroborated the retention of gelatine upon setting. The skeletal density of the reference material (α-TCP/water) was 2.84 ± 0.01 g ml^{-1}, consistent with a CDHA (the theoretical density of stoichiometric HA is 3.14 g ml^{-1}). With the incorporation of gelatine (skeletal density 1.34 g ml^{-1}), the skeletal density decreased to 2.74 ± 0.03 g ml^{-1}, and no statistically significant differences were found between non-crosslinked and crosslinked samples ($p > 0.05$). This value is in the range of the calculated densities assuming a release of 48.69 and 22.08% of the gelatine respectively for the non-crosslinked and crosslinked samples, which are 2.74 and 2.71 g ml^{-1} respectively. The SSAs of the crosslinked and non-crosslinked scaffolds were 22.88 ± 0.03 and 24.85 ± 0.02 m^2 g^{-1} respectively, which are well above the values reported in the literature for sintered HA scaffolds (below 2 m^2 g^{-1}).[32] This is considered as an advantage of the biomimetic self-setting scaffolds, since the high SSA, together with the lower crystallinity and non-stoichiometry of the CDHA,[14] contributes to a higher reactivity, and therefore a higher resorption rate is to be expected.

3.4. Mechanical characterisation

Immediately after printing, the scaffolds exhibited a flexible elastic behaviour, similar to gelatine hydrogels,[33] as shown in Fig. 7a and the inset. The mechanical behaviour was strongly modified after setting, with a transition from the viscoelastic hydrogel-like behaviour to a brittle ceramic-like behaviour. Thus, there was a significant increase of the compressive strength and a one hundred-fold increase of the stiffness, together with a decrease of the strain to failure (Fig. 7a). This can be explained by the mechanical interlocking of the precipitated crystals formed during the setting reaction, the mechanism behind the hardening of apatitic calcium phosphate cements.[14] Whereas before setting the ceramic particles were not bond to each other (Fig. 4b), the continuous matrix being the hydrogel, after setting a continuous matrix of ceramic crystals was formed (Fig. 4c), and therefore the ceramic behaviour prevailed. Crosslinking of the gelatine had a significant effect on the compressive strength of the scaffold, with a 76% increase, from 9.4 ± 1.6 MPa for non-crosslinked to 16.6 ± 3.2 MPa for crosslinked scaffolds.

This can be associated with the smaller micro/nanoporosity and pore size of the crosslinked samples, caused by the higher amount of gelatine retained within the inorganic

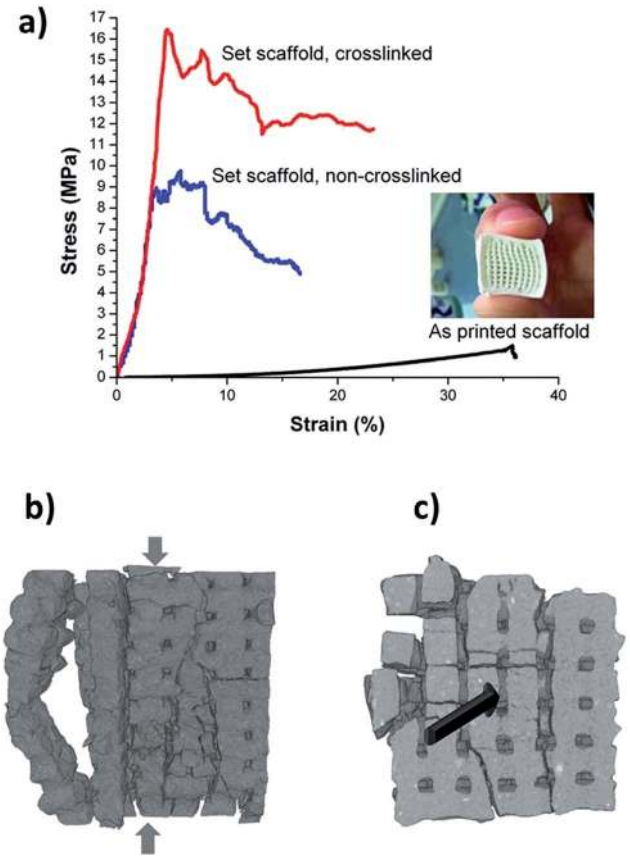

Fig. 7 (a) Stress–strain curves obtained during uniaxial compression tests performed on: (a) robocasted scaffolds, right after printing (black line), non-crosslinked set scaffolds (after 7 days of setting, blue line) and crosslinked set scaffolds (after 7 days of setting, red line). As shown in the inset, the scaffold was flexible and easily deformed elastically before setting; (b) lateral view and (c) vertical view of reconstructed broken scaffolds obtained by μ-CT scanning during an *in situ* uniaxial compression test (strain = 10%).

crystal network, as revealed by the MIP and SEM studies (Fig. 3 and 4d). This improvement of the mechanical strength was reported also in previous studies on gelatine-containing calcium phosphate cements.[15,17–19] In contrast, gelatine had no influence on the stiffness of the scaffolds, since no statistically significant differences ($p > 0.05$) were found between the elastic modulus of the crosslinked (240 ± 42 MPa) and non-crosslinked (227 ± 28 MPa) samples. This confirms that, once set, the continuous ceramic phase determines the mechanical behaviour of the scaffold. As expected, the compressive strength and elastic modulus of the scaffolds obtained with the self-setting ink lie below the levels reported in the literature for sintered robocasted hydroxyapatite scaffolds,[34] as a direct consequence of the intrinsic mechanical properties of CDHA obtained at low-temperature by a self-setting reaction, which has a higher micro/nanoporosity than high-temperature HA ceramics. However, our values are higher than those found in other low-temperature consolidated robocasted scaffolds[11] and, what is more interesting, both the elastic modulus and the compressive strength are within the range of

the human trabecular bone, 1–20 MPa and 10–500 MPa respectively.[35]

The *in situ* μ-CT imaging of the fracture under compression revealed that the set scaffolds presented the same fracture pattern as sintered robocasted scaffolds (Fig. 7b and c),[34,36] which are known to break by the splitting of the pillar arrays constituted by the piled crisscrossing of the successive deposited layers. The pillars are solicited in compression until a first pillar fails because of the propagation of cracks perpendicularly to both strand directions.[36] Subsequently, the bridges between pillars are solicited in flexural mode, and a combined failure of the bridges linking the pillars occurs, splitting one or more pillars at a time. The first pillars to fail were found on the outer part of the scaffold, due to the lower number of linkages linking them to other pillars.

3.5. Rat mesenchymal stem cell adhesion and proliferation

Adhesion and proliferation of rMSCs on the surface of set α-TCP/gelatine and α-TCP/water discs are shown in Fig. 8. After 5 h of culture, lower number of cells were observed in all samples compared to TCPS. This behaviour has been previously described for this kind of low-temperature apatites, and attributed to either topographical or ionic exchange effects.[37–39] It is noteworthy that, a higher number of cells ($p < 0.05$) adhered on the surface of the discs containing crosslinked gelatine than on those with non-crosslinked gelatine or the reference inorganic discs. This was consistent with the uneven detection of gelatine in the crosslinked and non-crosslinked samples, as shown in Fig. 4c and d, and was probably caused by the high density of RGD sequences[23] exposed on the surface of the crosslinked samples promoting the early attachment of cells.[40] SEM images showing good cell spreading on the different materials after 5 h of culture are shown in the ESI, Fig. S3.† However, after 24 h of culture there were no differences in cell adhesion between both discs containing crosslinked and non-crosslinked gelatine. At longer culture times (7 days), continuous cell proliferation was found only on the discs containing crosslinked gelatine, which is consistent with previous results obtained with gelatine-containing calcium phosphate foams[41] and microspheres.[16] In contrast, a delayed cell proliferation was observed in the case of discs containing non-crosslinked gelatine.[37] The present work suggests that the presence of crosslinked gelatine accelerated not only cell adhesion but also cell proliferation on hydroxyapatite discs. These results proved also that the crosslinking process did not compromise the cytocompatibility of the material. Another relevant aspect is that not only the chemistry, but also the surface topography was different in the two robocasted scaffolds. There is extensive literature that indicates that different cell responses can be expected towards hydroxyapatite substrates with varying micro and nanoscale surface topographies[37,42] as the ones developed in the present study, and work in this direction is under way in our laboratories.

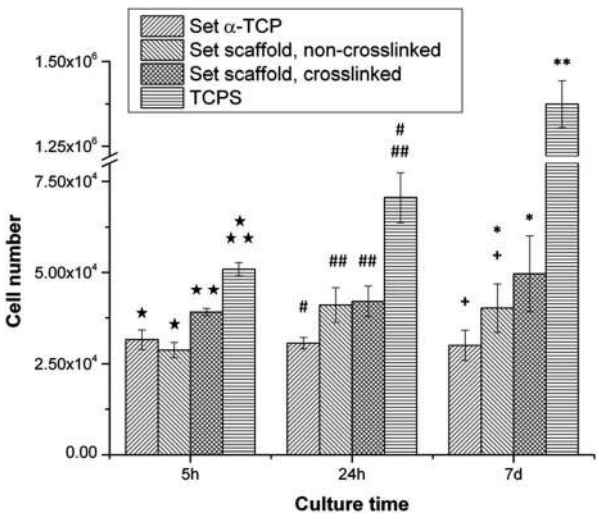

Fig. 8 Rat mesenchymal stem cell adhesion and proliferation over a 7 day period on discs of the set samples (non-crosslinked and crosslinked), as well as the reference set α-TCP without gelatine and TCPS used as the control. The same symbols indicate no statistically significant differences ($p > 0.05$) between groups at that time point.

4. Conclusions

Hydroxyapatite/gelatine scaffolds that mimic the chemical, structural and mechanical features of bone tissue were obtained by robocasting, using low-temperature self-setting α-TCP/gelatine inks. α-TCP was converted into CDHA upon setting in water, and gelatine was effectively retained by chemical crosslinking. The scaffolds exhibited a multimodal macro/micro/nanoporous architecture. The compressive strength of the robocasted scaffolds increased significantly upon setting, and a further increase was registered upon gelatine crosslinking. The set robocasted scaffolds exhibited compressive strength and elastic modulus in the range of the human trabecular bone. The presence of gelatine also enhanced mesenchymal stem cell adhesion and proliferation. In conclusion, the strategy of combining additive manufacturing techniques with low-temperature setting ceramic systems opens new perspectives for the fabrication of ceramic and hybrid 3D structures with controlled architectures from the nano to the macroscale, which can be exploited both in bone tissue engineering and in drug delivery applications.

Acknowledgements

The authors acknowledge the Spanish Government for financial support through the MAT2012-38438-C03 project and the Swedish Foundation for International Cooperation in Research and Higher Education (STINT, GA IG2011-2047). YM acknowledges the Spanish PhD grant no. AP2010-4051. Support for the research of MPG was received through the prize "ICREA Academia" for excellence in research, funded by the Generalitat de Catalunya. The authors are also grateful to F. J. Martinez-Vazquez, P. Miranda and A. Pajares (Universidad de Extremadura) and M. Navarro and T. Serra (the Institute for Bioengineering of Catalonia) for their help with robocasting fabrication.

References

1 V. Karageorgiou and D. Kaplan, *Biomaterials*, 2005, **26**, 5474–5491.
2 J. A. Lewis, J. E. Smay, J. Stuecker and J. Cesarano, *J. Am. Ceram. Soc.*, 2006, **89**, 3599–3609.
3 J. Lewis, *J. Am. Ceram. Soc.*, 2000, **59**, 2341–2359.
4 P. Miranda, E. Saiz, K. Gryn and A. P. Tomsia, *Acta Biomater.*, 2006, **2**, 457–466.
5 J. Franco, P. Hunger, M. E. Launey, A. P. Tomsia and E. Saiz, *Acta Biomater.*, 2010, **6**, 218–228.
6 Q. Fu, E. Saiz and A. P. Tomsia, *Adv. Funct. Mater.*, 2011, **21**, 1058–1063.
7 J. L. Simon, S. Michna, J. A. Lewis, E. D. Rekow, V. P. Thompson, J. E. Smay, A. Yampolsky, J. R. Parsons and J. L. Ricci, *J. Biomed. Mater. Res., Part A*, 2007, **83**, 747–758.
8 M. P. Ginebra, M. Espanol, E. B. Montufar, R. A. Perez and G. Mestres, *Acta Biomater.*, 2010, **6**, 2863–2873.
9 M. P. Ginebra, C. Canal, M. Espanol, D. Pastorino and E. B. Montufar, *Adv. Drug Delivery Rev.*, 2012, **64**, 1090–1110.
10 M. G. Li, X. Y. Tian and X. B. Chen, *Biofabrication*, 2009, **1**, 032001.
11 A. Lode, K. Meissner, Y. Luo, F. Sonntag, S. Glorius, B. Nies, C. Vater, F. Despang, T. Hanke and M. Gelinsky, *J. Tissue Eng. Regener. Med.*, DOI: 10.1002/term.1563, Epub ahead of print.
12 Y. Luo, A. Lode, F. Sonntag, B. Nies and M. Gelinsky, *J. Mater. Chem. B*, 2013, **1**, 4088–4098.
13 E. B. Montufar, Y. Maazouz and M. P. Ginebra, *Acta Biomater.*, 2013, **9**, 6188–6198.
14 M. P. Ginebra, E. Fernández, E. A. De Maeyer, R. M. Verbeeck, M. G. Boltong, J. Ginebra, F. C. Driessens and J. A. Planell, *J. Dent. Res.*, 1997, **76**, 905–912.
15 E. B. Montufar, T. Traykova, E. Schacht, L. Ambrosio, M. Santin, J. A. Planell and M. P. Ginebra, *J. Mater. Sci.: Mater. Med.*, 2010, **21**, 863–869.
16 R. A. Perez, S. Del Valle, G. Altankov and M. P. Ginebra, *J. Biomed. Mater. Res., Part B*, 2011, **97**, 156–166.
17 A. Bigi, B. Bracci and S. Panzavolta, *Biomaterials*, 2004, **25**, 2893–2899.
18 A. Bigi, I. Cantelli, S. Panzavolta and K. Rubini, *J. Appl. Biomater. Biomech.*, 2004, **2**, 81–87.
19 M.-Y. Shie, D. C.-H. Chen, C.-Y. Wang, T.-Y. Chiang and S.-J. Ding, *Acta Biomater.*, 2008, **4**, 646–655.
20 S.-J. Ding and M.-Y. Shie, *Adv. Eng. Mater.*, 2011, **13**, B246–B255.
21 G. E. Davis, *Biochem. Biophys. Res. Commun.*, 1992, **182**, 1025–1031.
22 M. H. Zaman, *Biophys. J.*, 2007, **92**, L17–L19.
23 S.-C. Wu, W.-H. Chang, G.-C. Dong, K.-Y. Chen, Y.-S. Chen and C.-H. Yao, *J. Bioact. Compat. Polym.*, 2011, **26**, 565–577.
24 M. C. Gómez-Guillén, B. Giménez, M. E. López-Caballero and M. P. Montero, *Food Hydrocolloids*, 2011, **25**, 1813–1827.
25 M. Djabourov, J. Leblond and P. Papon, *J. Phys.*, 1988, **49**, 333–343.
26 J. W. Mwangi and C. M. Ofner, *Int. J. Pharm.*, 2004, **278**, 319–327.
27 M. Espanol, R. A. Perez, E. B. Montufar, C. Marichal, A. Sacco and M. P. Ginebra, *Acta Biomater.*, 2009, **5**, 2752–2762.
28 M. P. Ginebra, F. C. M. Driessens and J. A. Planell, *Biomaterials*, 2004, **25**, 3453–3462.
29 M. Espanol, J. Portillo, J. M. Manero and M. P. Ginebra, *CrystEngComm*, 2010, **12**, 3318–3326.
30 E. Pretsch, *Determinación estructural de compuestos orgánicos*, Masson, Barcelona, 2002.
31 J. Siepmann and N. A. Peppas, *Int. J. Pharm.*, 2011, **418**, 6–12.
32 Y. C. Chai, A. Carlier, J. Bolander, S. J. Roberts, L. Geris, J. Schrooten, H. Van Oosterwyck and F. P. Luyten, *Acta Biomater.*, 2012, **8**, 3876–3887.
33 D. Kai, M. P. Prabhakaran, B. Stahl, M. Eblenkamp, E. Wintermantel and S. Ramakrishna, *Nanotechnology*, 2012, **23**, 095705.
34 P. Miranda, A. Pajares, E. Saiz, A. P. Tomsia and F. Guiberteau, *J. Biomed. Mater. Res., Part A*, 2008, **85**, 218–227.
35 S. A. Goldstein, *J. Biomech.*, 1987, **20**, 1055–1061.
36 P. Miranda, A. Pajares, E. Saiz, A. P. Tomsia and F. Guiberteau, *J. Biomed. Mater. Res., Part A*, 2007, **83**, 646–655.
37 E. Engel, S. Del Valle, C. Aparicio, G. Altankov, L. Asin, J. A. Planell and M. P. Ginebra, *Tissue Eng., Part A*, 2008, **14**, 1341–1351.
38 T. Yuasa, Y. Miyamoto, K. Ishikawa, M. Takechi, Y. Momota, S. Tatehara and M. Nagayama, *Biomaterials*, 2004, **25**, 1159–1166.
39 S. Sethuraman, L. S. Nair, S. El-Amin, M.-T. N. Nguyen, Y. E. Greish, J. D. Bender, P. W. Brown, H. R. Allcock and C. T. Laurencin, *J. Biomed. Mater. Res., Part A*, 2007, **82**, 884–891.
40 B. N. Grover, J. H. Gwynne, N. Pugh, S. Hamaia, R. W. Farndale, S. M. Best and R. E. Cameron, *Acta Biomater.*, 2012, **8**, 3080–3090.
41 E. B. Montufar, T. Traykova, J. A. Planell and M. P. Ginebra, *Mater. Sci. Eng., C*, 2011, **31**, 1498–1504.
42 D. O. Costa, P. D. H. Prowse, T. Chrones, S. M. Sims, D. W. Hamilton, A. S. Rizkalla and S. J. Dixon, *Biomaterials*, 2013, **34**, 7215–7226.

